# ICAM-1 induced rearrangements of capsid and genome prime rhinovirus 14 for activation and uncoating

Dominik Hrebík[a], Tibor Füzik[a], Mária Gondová[a], Lenka Šmerdová[a], Athanassios Adamopoulos[a], Ondrej Šedo[a], Zbyněk Zdráhal[a], and Pavel Plevka[a,1]

[a]Central European Institute of Technology, Masaryk University, Brno 62500, Czech Republic

Edited by Stephen C. Harrison, Boston Children's Hospital, Boston, MA, and approved April 4, 2021 (received for review November 23, 2020)

**Most rhinoviruses, which are the leading cause of the common cold, utilize intercellular adhesion molecule-1 (ICAM-1) as a receptor to infect cells. To release their genomes, rhinoviruses convert to activated particles that contain pores in the capsid, lack minor capsid protein VP4, and have an altered genome organization. The binding of rhinoviruses to ICAM-1 promotes virus activation; however, the molecular details of the process remain unknown. Here, we present the structures of virion of rhinovirus 14 and its complex with ICAM-1 determined to resolutions of 2.6 and 2.4 Å, respectively. The cryo-electron microscopy reconstruction of rhinovirus 14 virions contains the resolved density of octanucleotide segments from the RNA genome that interact with VP2 subunits. We show that the binding of ICAM-1 to rhinovirus 14 is required to prime the virus for activation and genome release at acidic pH. Formation of the rhinovirus 14–ICAM-1 complex induces conformational changes to the rhinovirus 14 capsid, including translocation of the C termini of VP4 subunits, which become poised for release through pores that open in the capsids of activated particles. VP4 subunits with altered conformation block the RNA–VP2 interactions and expose patches of positively charged residues. The conformational changes to the capsid induce the redistribution of the virus genome by altering the capsid–RNA interactions. The restructuring of the rhinovirus 14 capsid and genome prepares the virions for conversion to activated particles. The high-resolution structure of rhinovirus 14 in complex with ICAM-1 explains how the binding of uncoating receptors enables enterovirus genome release.**

virus | structure | receptor | cryo-electron microscopy | genome release

Human rhinoviruses are the cause of more than half of common colds (1). Medical visits and missed days of school and work cost tens of billions of US dollars annually (2, 3). There is currently no cure for rhinovirus infections, and the available treatments are only symptomatic. Rhinoviruses belong to the family *Picornaviridae*, genus *Enterovirus*, and are classified into species A, B, and C (4). Rhinoviruses A and B can belong to either "major" or "minor" groups, based on their utilization of intercellular adhesion molecule-1 (ICAM-1) or low-density lipoprotein receptor for cell entry (5–7). Type C rhinoviruses use CDHR3 as a receptor (8). Rhinovirus 14 belongs to the species rhinovirus B and uses ICAM-1 as a receptor. Receptors recognized by rhinoviruses and other enteroviruses can be divided into two groups based on their function in the infection process (9). Attachment receptors such as DAF, PSGL1, KREMEN1, CDHR3, and sialic acid enable the binding and endocytosis of virus particles into cells (10–13). In contrast, uncoating receptors including ICAM-1, CD155, CAR, and SCARB2 enable virus cell entry but also promote genome release from virus particles (5, 14–16).

Virions of rhinoviruses are nonenveloped and have icosahedral capsids (17). Genomes of rhinoviruses are 7,000 to 9,000 nucleotide-long single-stranded positive-sense RNA molecules (1, 17). The rhinovirus genome encodes a single polyprotein that is co- and posttranslationally cleaved into functional protein subunits. Capsid proteins VP1, VP3, and VP0, originating from one polyprotein, form a protomer, 60 of which assemble into a pseudo-T = 3 icosahedral capsid. To render the virions mature and infectious, VP0 subunits are cleaved into VP2 and VP4 (18, 19). VP1 subunits form pentamers around fivefold symmetry axes, whereas subunits VP2 and VP3 form heterohexamers centered on threefold symmetry axes. The major capsid proteins VP1 through 3 have a jelly roll β-sandwich fold formed by two β-sheets, each containing four antiparallel β-strands, which are conventionally named B to I (20–22). The two β-sheets contain the strands BIDG and CHEF, respectively. The C termini of the capsid proteins are located at the virion surface, whereas the N termini mediate interactions between the capsid proteins and the RNA genome on the inner surface of the capsid. VP4 subunits are attached to the inner face of the capsid formed by the major capsid proteins. The surfaces of rhinovirus virions are characterized by circular depressions called canyons, which are centered around fivefold symmetry axes of the capsids (21).

The VP1 subunits of most rhinoviruses, but not those of rhinovirus 14, contain hydrophobic pockets, which are filled by molecules called pocket factors (17, 21, 23, 24). It has been speculated that pocket factors are fatty acids or lipids (25). The pockets are positioned immediately below the canyons. The exposure of rhinoviruses to acidic pH induces expulsion of the pocket factors, which leads to the formation of activated particles and genome release (17, 26–32). The activated particles are characterized by capsid expansion, a reduction in interpentamer contacts, the release of VP4 subunits, externalization of N termini of VP1 subunits, and changes in the distribution of RNA genomes (17, 26–29, 33, 34). Artificial hydrophobic compounds that bind to VP1 pockets with high affinity inhibit infection by rhinoviruses (35, 36).

ICAM-1 is an endothelial- and leukocyte-associated protein that stabilizes cell–cell interactions and facilitates the movement

## Significance

**Medical visits and missed days of school and work caused by rhinoviruses cost tens of billions of US dollars annually. Currently, there are no antivirals against rhinoviruses, and the available treatments only treat the symptoms. Here, we present the molecular structure of human rhinovirus 14 in complex with its cellular receptor intercellular adhesion molecule 1. The binding of the virus to its receptor initiates the infection. Knowledge of the structure of the human rhinovirus 14–intercellular adhesion molecule 1 interface and mechanism of interaction provides the basis for the design of compounds that may block the binding of rhinoviruses to receptors and thus prevent infection.**

Author contributions: D.H. and P.P. designed research; D.H., L.Š., A.A., and O.Š. performed research; D.H., T.F., M.G., O.Š., Z.Z., and P.P. analyzed data; and D.H., T.F., and P.P. wrote the paper.

The authors declare no competing interest.

This article is a PNAS Direct Submission.



[1]To whom correspondence may be addressed. Email: pavel.plevka@ceitec.muni.cz.

This article contains supporting information online at https://www.pnas.org/lookup/suppl/doi:10.1073/pnas.2024251118/-/DCSupplemental.

Published May 5, 2021.

of leukocytes through endothelia (37). ICAM-1 can be divided into an extracellular amino-terminal part composed of five immunoglobulin domains, a single transmembrane helix, and a 29-residue–long carboxyl-terminal cytoplasmic domain. The immunoglobulin domains are characterized by a specific fold that consists of seven to eight β-strands, which form two antiparallel β-sheets in a sandwich arrangement (38–40). The immunoglobulin domains of ICAM-1 are stabilized by disulfide bonds and glycosylation (38–41). The connections between the immunoglobulin domains are formed by flexible linkers that enable bending of the extracellular part of ICAM-1. For example, the angle between domains 1 and 2 differs by 8° between molecules in distinct crystal forms (38, 42). As a virus receptor, ICAM-1 enables the virus particles to sequester at the cell surface and mediates their endocytosis (5). The structures of complexes of rhinoviruses 3, 14, and 16, and CVA21 with ICAM-1 have been determined to resolutions of 9 to 28 Å (42–46). It was shown that ICAM-1 molecules bind into the canyons at the rhinovirus surface, approximately between fivefold and twofold symmetry axes (42–46). ICAM-1 interacts with residues from all three major capsid proteins. It has been speculated that the binding of ICAM-1 triggers the transition of virions of rhinovirus 14 to activated particles and initiates genome release (45, 47). However, the limited resolution of the previous studies prevented characterization of the corresponding molecular mechanism.

Here, we present the cryo-electron microscopy (cryo-EM) reconstruction of the rhinovirus 14 virion, which contains resolved density of octanucleotide segments of the RNA genome that interact with VP2 subunits. Furthermore, we show that the binding of ICAM-1 to rhinovirus 14 induces changes in its capsid and genome, which are required for subsequent virus activation and genome release at acidic pH.

## Results and Discussion

**Interactions of Capsid of Rhinovirus 14 with Genome.** The cryo-EM reconstruction of rhinovirus 14 virion was determined to a resolution of 2.6 Å (Fig. 1 *A* and *B* and *SI Appendix*, Fig. S1 and Table S1). The map enabled building of the structure of capsid proteins VP1 through 4 except for residues 1 to 17 and 290 to 293 of VP1, 1 to 6 of VP2, and 1 to 28 of VP4 (Fig. 1*B*). In addition to the capsid, the cryo-EM map contains resolved density corresponding to octanucleotide segments from the RNA genome (Fig. 1 *A*–*C*). The quality of the map enabled building of the RNA structure; however, the nucleotide sequence could not be identified. The base of the second nucleotide from the 5′ end of the RNA segment is flipped out from the RNA helix and forms a stacking interaction with the sidechain of Trp38 of VP2 (Fig. 1*D* and *SI Appendix*, Fig. S2). The residue Trp38 is conserved in the VP2 subunits of numerous picornaviruses, including polioviruses, rhinoviruses 2 and 16, coxsackievirus B3, coxsackievirus A9, and coxsackievirus A21 (*SI Appendix*, Fig. S3). Virion structures of these viruses contain disk-like densities that stack onto the tryptophane side chains, which were hypothesized to belong to a base of guanine nucleotide (23, 24, 48–51). The structure of the RNA segment in the virion of rhinovirus 14 provides evidence that the previous speculations about the densities stacking onto Trp38 side chains were correct. To be consistent with the previous structures, we modeled the second nucleotide of the RNA segment in rhinovirus 14 as guanine (Fig. 1*D* and *SI Appendix*, Fig. S2). The stacking interaction between Trp38 and the base of the second nucleotide is the only direct contact between the RNA segment and the capsid (Fig. 1 *A*, *C*, and *D* and *SI Appendix*, Fig. S2).

Each RNA segment in the virion of rhinovirus 14 is associated with one protomer of capsid proteins VP1 through 4 (Fig. 1 *A* and *B*). The RNA is positioned next to a twofold axis, and two of the oligonucleotides interact with each other (Fig. 1 *A*–*C*). To enable Watson–Crick base pairing between the two segments, the nucleotide at position seven was modeled as uracil and the nucleotide at position eight as adenine (Fig. 1*C*). Due to the constraints imposed by the interaction of the RNA with the capsid and of the interactions of two segments of the RNA with each other, the sequence of the oligonucleotide was built as 5′ UGUUUUUA 3′. Nevertheless, other sequences that fulfill the interaction conditions are equally possible.

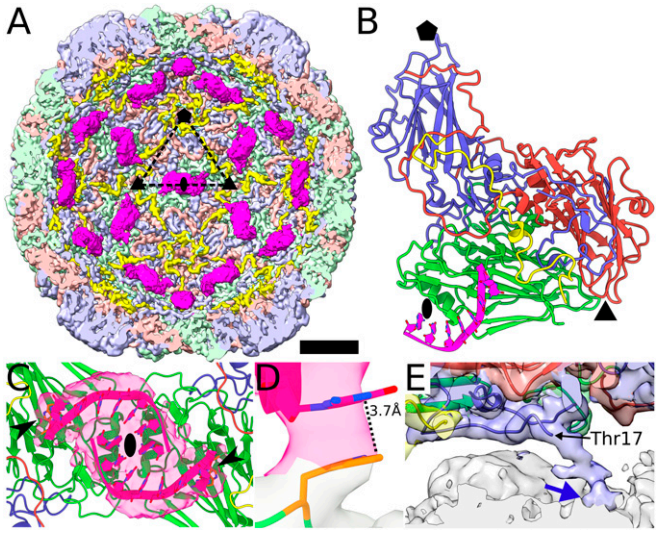


**Fig. 1.** Structure of virion of rhinovirus 14 contains resolved density corresponding to octanucleotides from its RNA genome. (*A*) Surface representation of cryo-EM of reconstruction of virion of rhinovirus 14 with front half of the particle removed to show internal structure. Density corresponding to VP1 is shown in blue, VP2 in green, VP3 in red, VP4 in yellow, and RNA segments in pink. Borders of a selected icosahedral asymmetric unit are indicated with a dashed triangle and positions of selected twofold, threefold, and fivefold symmetry axes are represented by an oval, triangle, and pentagon, respectively. (Scale bar, 5 nm.) (*B*) Cartoon representation of icosahedral asymmetric unit of rhinovirus 14 viewed from the inside of the capsid. The color coding of individual virus components is the same as in *A*. Positions of twofold, threefold, and fivefold symmetry axes are represented by an oval, triangle, and pentagon, respectively. (*C*) Two RNA octanucleotides that interact with each other and with VP2 subunits. Protein and RNA coloring is the same as in *A*. The cryo-EM density of the RNA segments is shown as a pink semitransparent surface. RNA bases and side chains of Trp38 of VP2 are shown in stick representation, in orange, and indicated with black arrowheads. The position of a twofold symmetry axis is indicated with an oval. (*D*) Detail of stacking interaction between Gua2 from RNA segment and Trp38 of VP2. The cryo-EM densities of RNA and protein are shown as semitransparent surfaces in pink and gray, respectively. (*E*) Interaction between N terminus of VP1 and genome. Capsid proteins are shown in cartoon representation with the same coloring as in *A*. Cryo-EM densities of individual proteins are shown as semitransparent surfaces colored according to the chain they belong to. The density of the RNA genome is shown in gray. The blue arrow indicates the contact between the N terminus of VP1 and the genome. The position of Thr17, the first modeled residue from the N terminus of VP1, is indicated.

The reconstruction of virion of rhinovirus 14 provides evidence that the N termini of VP1 subunits interact with the RNA genome (Fig. 1*E*). A similar function of the N terminus of VP1 was described previously in rhinovirus 2 (26). None of the interactions between the genomes and capsids of enteroviruses identified to date are sequence specific. Nevertheless, even the nonspecific interactions of the N termini of VP1 and Trp38 of VP2 with the RNA may enable the packaging of the enterovirus genome into a particle. Compounds that could prevent the RNA–capsid interaction by, for instance covering the side chain of Trp38, may interfere with the production of infectious virions.

**Binding of Rhinovirus 14 to ICAM-1 Does Not Induce Genome Release.** The complex of rhinovirus 14 with ICAM-1 was prepared by mixing the components in phosphate-buffered saline (PBS) of

pH 7.4 and incubating them at 34 °C for 30 min (Fig. 2). The temperature was chosen to mimic that in the human upper respiratory tract (52). The binding of ICAM-1 did not induce the formation of activated particles or the genome release of rhinovirus 14 (Fig. 2 *A*–*C*). This is in agreement with previous results showing that the ability of ICAM-1 to trigger genome release depends on temperature, receptor concentration, and buffer composition (47, 53). Experiments showing that ICAM-1 could induce genome release were performed in solutions with nonphysiological concentrations of salts, which may have destabilized the virus particles (42, 46, 47). Since enteroviruses have to deliver their genomes into the cytoplasm of a host cell to initiate infection, it would be detrimental if they released their genomes immediately upon binding to receptors at the cell surface. Our results show that rhinovirus 14 is stable when bound to ICAM-1 under native-like conditions (Fig. 2*C*), and the induction of genome release requires exposure to acidic pH in endosomes.

**Structure of Rhinovirus 14–ICAM-1 Complex.** The structure of rhinovirus 14 in complex with the soluble ectodomain of ICAM-1 was determined to a resolution of 2.4 Å using cryo-EM and single-particle reconstruction (Fig. 3 and*SI Appendix*, Fig. S1 and Table S1). Domain 1 of ICAM-1 bound at the surface of rhinovirus 14 was resolved to a resolution of 2.6 Å (Fig. 3*A* and *SI Appendix*, Fig. S1). Levels of density in the map region corresponding to the domain 1 of ICAM-1 are similar to those in the capsid of the virus, indicating full occupancy of the receptors at the virus surface. Domains 2 and 3 of ICAM-1 are resolved to a resolution of 6 Å, and domains 4 and 5 are not visible in the cryo-EM reconstruction (Fig. 3*A*). The low resolution of the region of the map corresponding to domains 2 and 3 and the lack of density for domains 4 and 5 are probably caused by movements of those domains relative to domain 1, which is anchored at the virus surface (Fig. 3*A*) (38, 42, 43). In agreement with previous studies, domain 1 of ICAM-1 binds into the canyon of rhinovirus 14, approximately in the middle between fivefold and twofold symmetry axes (Fig. 3 *B* and *C*) (42, 43, 45). Previous studies of the interactions of rhinoviruses 3, 14, and 16 with ICAM-1 were limited to a resolution of 9.5 Å or lower (42–46). The interpretation of the macromolecular interactions relied on the fitting of high-resolution structures, determined by X-ray crystallography, to the cryo-EM maps of the complex (42–46). Therefore, the changes in the structures of the receptor and virus, induced upon their binding, could not be identified. Here, we show that ICAM-1 is wedged 3.4 Å deeper into the canyon and rotated 7.6° clockwise, when looking along the long axis of domain 1 toward the virus surface, relative to the structure reported previously (Fig. 4 and *SI Appendix*, Fig. S4*A*) (42, 43, 45). The interaction interface between ICAM-1 and rhinovirus 14 has a buried surface area of 1,500 $Å^2$. The core of domain 1 of ICAM-1 is formed by β-sheets ABED and GFC (Fig. 4 *A*–*C*) (11, 54). Residues from the loops BC, DE, and FG and strands B, C, D, E, F, and G of ICAM-1 interact with rhinovirus 14 (*SI Appendix*, Fig. S4*B*). The mode of attachment of rhinovirus 14 to ICAM-1 is characteristic for uncoating receptors that bind to enterovirus canyons (5, 9, 14, 15). The uncoating receptors of enteroviruses, including ICAM-1, CD155, and CAR, have elongated molecules formed by domains with an immunoglobulin



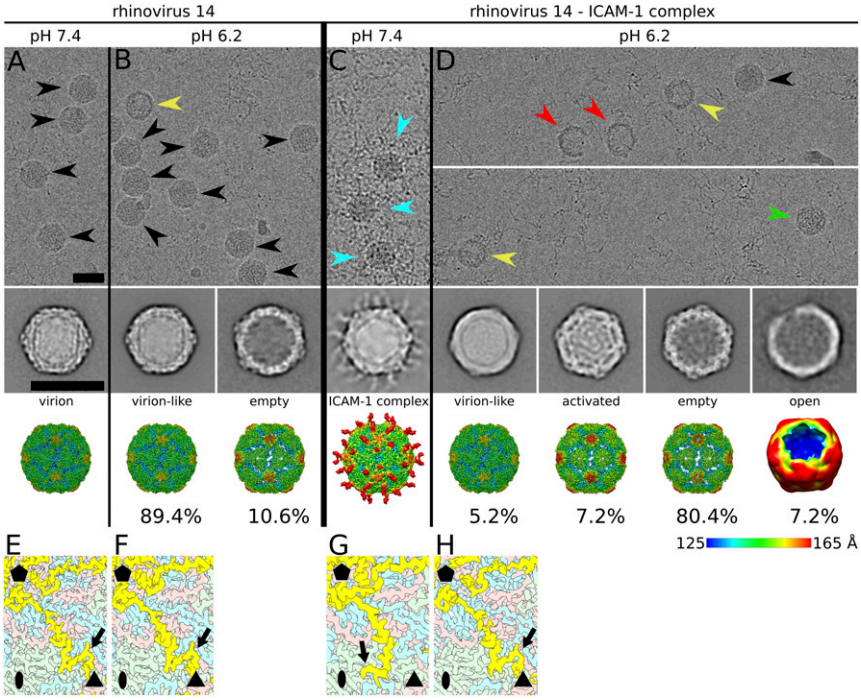


**Fig. 2.** Binding of ICAM-1 to rhinovirus 14 is required for efficient genome release at acidic pH. (*A*–*D*) Electron micrographs (*Top*), reference-free two-dimensional class averages (*Center*), and 3D reconstructions (*Bottom*) of rhinovirus 14 and rhinovirus 14–ICAM-1 complex at neutral and acidic pH. The cryo-EM reconstructions are rainbow colored based on the distance of the particle surface from its center. Names above the reconstructions indicate the types of particles. Percentages below the reconstructions indicate the relative abundance of each type of particle in the sample. (*A* and *B*) Rhinovirus 14 at pH 7.4 (*A*) and 6.2 (*B*). (*C* and *D*) Rhinovirus 14–ICAM-1 complex at pH 7.4 (*C*) and 6.2 (*D*). The top row of *D* contains two parts of a micrograph to show all types of particles present in the sample. Black arrowheads indicate virions, yellow indicate empty particles, cyan indicate rhinovirus 14–ICAM-1 complex, green indicate activated particles, and red indicate open particles. (Scale bars, 30 nm.) (*E*–*H*) Conformational changes to VP4 are induced by ICAM-1 binding but not by acidic pH. Surface representations of cryo-EM reconstructions showing the inner faces of capsids. The surfaces are color coded according to the capsid proteins with VP1 in blue, VP2 in green, VP3 in red, and VP4 in yellow. Only particles containing VP4 are shown. Positions of icosahedral symmetry axes are indicated with a black pentagon, triangle, and oval for fivefold, threefold, and twofold, respectively. Black arrows highlight C termini of VP4.

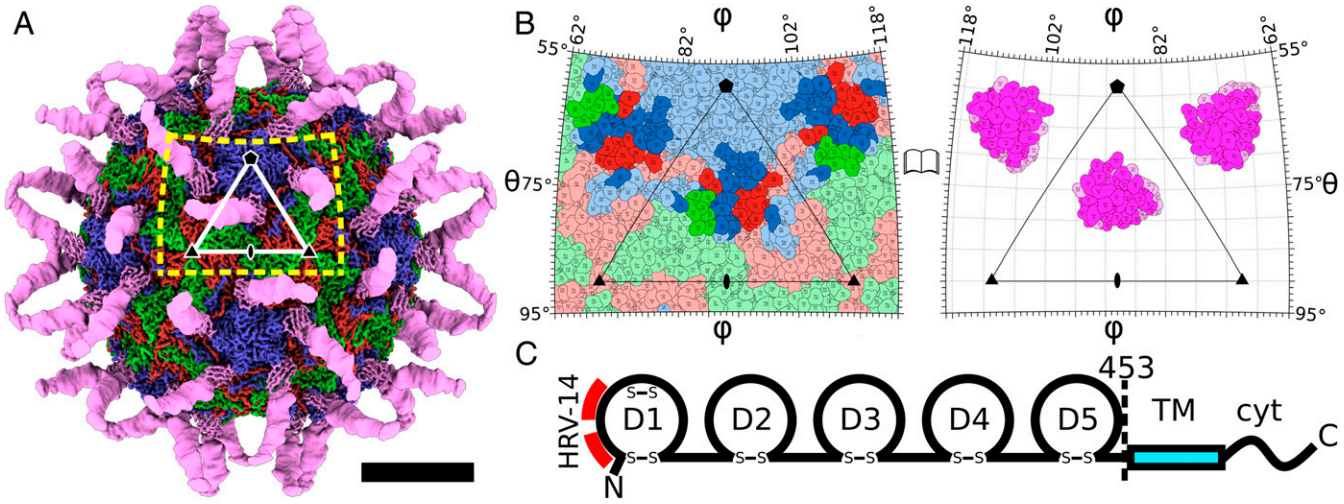


**Fig. 3.** Structure of rhinovirus 14 in complex with ICAM-1. (*A*) Surface representation of cryo-EM reconstruction of rhinovirus 14–ICAM-1 complex color coded to distinguish individual proteins. Density corresponding to VP1 is shown in blue, VP2 in green, VP3 in red, and ICAM-1 in light magenta. Positions of selected icosahedral symmetry axes are indicated by a pentagon for fivefold, triangle for threefold, and an oval for twofold. The white triangle indicates the border of a selected icosahedral asymmetric unit. The yellow dashed rectangle indicates borders of the area shown in detail in *B*. (*B*) Roadmap projection showing residues forming the outer surface of rhinovirus 14 capsid (*Left*) and residues of domain 1 of ICAM-1 facing toward the virus (*Right*). Coloring is the same as in *A*. Residues involved in virus–receptor interactions are shown in bright colors. The polar angles θ and ϕ indicate positions at the capsid surface. (*C*) Schematic representation of ICAM-1. D1 to D5 indicate extracellular immunoglobulin domains; TM, transmembrane domain; cyt, cytoplasmic domain. Disulfide bridges (S-S) stabilizing the immunoglobulin domains are indicated. Red dashes highlight the binding site for rhinovirus 14. The ectodomain used in this study to determine the rhinovirus 14–ICAM-1 interactions included residues 1 to 453.

fold, which enables their insertion into the canyons of enterovirus particles (5, 14, 15).

**Conformational Changes Required for Binding of Rhinovirus 14 to ICAM-1.** The binding of rhinovirus 14 to ICAM-1 is accompanied by the local restructuring of domain 1 of ICAM-1 and surface loops of capsid proteins, as well as by overall changes in the structure of the rhinovirus-14 capsid (Figs. 4 and 5 and *SI Appendix*, Figs. S5 and S6). VP1 subunits rotate 1.7° toward VP2 and VP3, which results in a contraction of the canyon (Fig. 4*A*). As a result, the capsid expands by 5 Å in diameter (Fig. 4*A*). The binding of ICAM-1 to rhinovirus 14 requires the bending of the FG loop of ICAM-1 8 Å toward the core of the immunoglobulin domain (Fig. 4*B* and *SI Appendix*, Fig. S5). This conformational change is necessary to prevent the clashing of the FG loop of ICAM-1 with residues 178 to 182 from the FG loop of VP3 of rhinovirus 14 (Fig. 4*B*). The conformational flexibility of the FG loop of ICAM-1 enables enlargement of its interaction interface with the capsid.

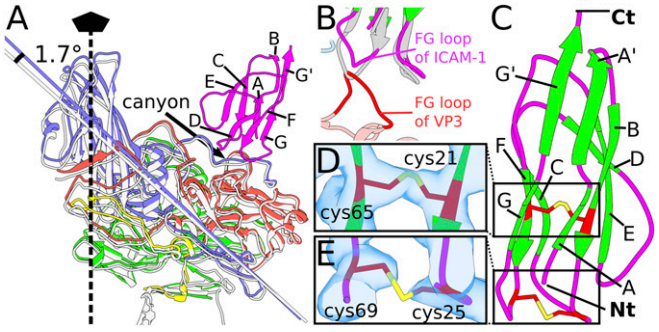


**Fig. 4.** Conformational changes associated with binding of rhinovirus 14 to ICAM-1. (*A*) Cartoon representation of icosahedral asymmetric unit of rhinovirus 14 in complex with ICAM-1. The VP1 subunit is shown in blue, VP2 in green, VP3 in red, VP4 in yellow, and domain 1 of ICAM-1 in magenta. The capsid proteins from virion of rhinovirus 14 are superimposed onto those of the rhinovirus 14–ICAM-1 complex and are shown in white. The binding of ICAM-1 to rhinovirus 14 induces a 1.7° tilt of VP1 toward VP2 and VP3, which results in a narrowing of the canyon relative to the virion structure. Least-squares planes fitted to VP1 are shown to highlight the rotation of VP1. (*B*) Conformational change of FG loop of ICAM-1, shown in magenta, is required to prevent clashes with FG loop of VP3, shown in red. The native structure of ICAM-1 clashing with VP2 is shown in gray. (*C*) Cartoon representation of structure of ICAM-1 bound to rhinovirus 14 with side chains of cysteine residues shown in stick representation with red carbon atoms and yellow sulfur atoms. (*D* and *E*) Detail of disulfide bridge between Cys21 and Cys65 (*D*) and Cys25 and Cys69 (*E*). Cryo-EM density is shown as a semitransparent blue surface.

The structures of domain 1 of ICAM-1 determined to date contain the disulfide bonds Cys21 and Cys65 and Cys25 and Cys69 (38–40). Residues Cys25 and Cys69 are located in the vicinity of the virus surface when ICAM-1 binds to rhinovirus 14 (Fig. 4 *C*–*E*). Cys69 is part of the FG loop, whereas Cys25 is part of the BC loop (Fig. 4 *C* and *E*). The density connecting Cys25 and Cys69 of ICAM-1 in the complex with rhinovirus 14 is much weaker than that connecting Cys21 to Cys65 (Fig. 4 *C* and *E*). However, the positions of the two cysteines in the cryo-EM density map are consistent with the linkage of their side chains by a disulfide bond (Fig. 4 *C* and *E*) (55). Furthermore, mass spectrometry analysis of ICAM-1 molecules from the complex with rhinovirus 14 did not detect any peptides containing free Cys25 and Cys69 (*SI Appendix*, Fig. S7). However, peptides containing free cysteines were observed after the reduction of the disulfide bonds by dithiothreitol (DTT). This provides evidence that Cys25 and Cys69 of ICAM-1 in complex with rhinovirus 14 are linked by a disulfide bond. The low values of cryo-EM density may be caused by a higher flexibility of this part of ICAM-1, as indicated by the lower resolution than in the core of domain 1 (Fig. 3*A*). The binding of rhinovirus 14 to ICAM-1 also induces structural changes in the virus proteins. Residues 154 to 162 from the DE loop of VP1 shift 2 Å toward the core of the subunit (*SI Appendix*, Fig. S6). This movement helps to accommodate ICAM-1 in the canyon of rhinovirus 14.

**Molecular Details of the Interface between Rhinovirus 14 and ICAM-1.** The interaction between ICAM-1 and rhinovirus 14 is formed by 36 residues from domain 1 of ICAM-1 and 31, 8, and 13 residues

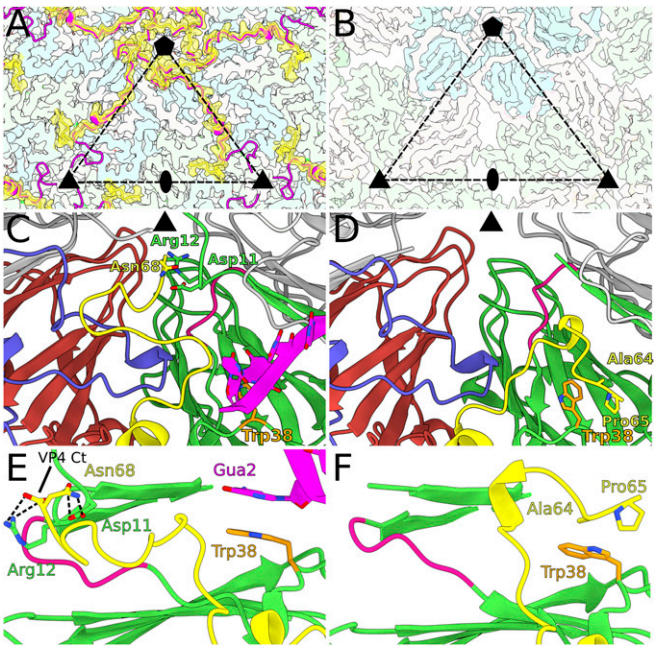


**Fig. 5.** Changes of structure of C terminus of VP4 induced by ICAM-1 binding to rhinovirus 14. (*A*) Surface representation of cryo-EM reconstruction of capsid of rhinovirus 14 in complex with ICAM-1 viewed from inside the virion. Density corresponding to VP1 is shown in pale blue, VP2 in pale green, VP3 in pale red, and VP4 in semitransparent yellow. The structure of VP4 in the rhinovirus 14–ICAM-1 complex is shown in cartoon representation in yellow, whereas the structure of VP4 in the virion of rhinovirus 14 is shown in magenta. The positions of selected icosahedral symmetry axes are indicated with a pentagon for fivefold, triangle for threefold, and oval for twofold. Borders of a selected icosahedral asymmetric unit are indicated with a dashed triangle. (*B*) Capsid structure of an empty particle of rhinovirus 14 containing pores around twofold symmetry axes and between twofold and fivefold symmetry axes through which VP4 may be released from the particle. (*C–F*) Differences in structure of VP4 subunits in virion (*C* and *E*) and rhinovirus 14–ICAM-1 complex (*D* and *F*). Capsid proteins are shown in cartoon representation. VP1 is shown in blue, VP2 in green, VP3 in red, VP4 in yellow, and RNA segments in pink. (*C* and *E*) Asn68 from C terminus of VP4 interacts with Asp11 and Arg12 of VP2 in virion of rhinovirus 14. The residues Asp11 and Arg12 are stabilized in position by the underlying loop of VP2 formed by residues 27 to 32 (highlighted in magenta). The side chain of Trp38 (highlighted in orange) forms a stacking interaction with Gua2 that is part of the resolved RNA segment positioned next to a twofold axis. (*D* and *F*) Binding of rhinovirus 14 to ICAM-1 induces conformational changes of virus capsid that include movement of residues 27 to 32 of VP2 toward particle center, which prevents interaction of C terminus of VP4 with residues Asp11 and Arg12 of VP2. The C terminus of VP4 acquires a new conformation, which covers the side chain of Trp38 of VP2 and blocks its interaction with RNA.

of VP1, VP2, and VP3 of rhinovirus 14, respectively (Fig. 3*B*). The specificity of the interaction is controlled by a combination of the complementarity of the electrostatic interactions, a network of hydrogen bonds, and the positions of patches of hydrophobic interfaces. There are salt bridges between Lys77 of ICAM-1 and Glu210 from VP1 and Lys39 of ICAM-1 and C-terminal carboxyl group of Glu236 from VP3 (*SI Appendix*, Fig. S8 *A* and *B*). The interface includes a network of 18 hydrogen bonds. Furthermore, the resolution of the cryo-EM reconstruction of the complex was sufficient to enable the identification of water molecules, some of which form hydrogen bonds with both ICAM-1 and rhinovirus 14 and thus mediate interactions between the receptor and virus (*SI Appendix*, Fig. S8 *C* and *D*). For example, the amino group from the side chain of Lys29 of ICAM-1 interacts with two water molecules that form hydrogen bonds with side chains of Thr105 of VP3 and Asn68 of ICAM-1 (*SI Appendix*, Fig. S8*D*). It has been shown previously that the mutation of Thr75 of ICAM-1 to Ala reduces the efficiency of binding of rhinovirus 14 by more than 50% (54, 56). No ions were identified at the rhinovirus 14–ICAM-1 interface (7, 57).

The interface between rhinovirus 14 and ICAM-1 contains complementary patches of hydrophobic interactions (*SI Appendix*, Fig. S8 *E* and *F*). Previous studies have shown that most mutations of Pro70 from the FG loop of ICAM-1 prevent the binding of rhinovirus 14 (54, 56). We show that Pro70 fits into a small hydrophobic pocket formed by Pro178, Phe86, and Thr180 of VP3 (*SI Appendix*, Fig. S8*F*). Fitting Pro70 of ICAM-1 into the hydrophobic cavity in VP3 requires movement and restructuring of the FG loop of ICAM-1 (Fig. 4 *C* and *E* and *SI Appendix*, Fig. S8*F*). Another residue of ICAM-1 that is critical for the binding of rhinovirus 14 is Leu30 (54, 56). In the complex, the side chain of Leu30 is situated between the side chains of Ile215 and Val217 from VP1, which form a hydrophobic pocket for the leucine side chain (*SI Appendix*, Fig. S8*E*). This explains why the mutation of Leu30 to Ser eliminates the binding of ICAM-1 to rhinovirus 14 (54, 56).

**ICAM-1 Binding Prepares VP4 Subunits for Release from Activated Particles.** The structure of the C terminus of VP4 subunit in the rhinovirus 14–ICAM-1 complex differs from that in the native virion (Figs. 2 *E–H* and 5). The two structures of VP4 subunits are similar for residues 29 to 57, with rmsd of Cα atoms of the corresponding residues of 0.44 Å. However, residues 58 to 65 of VP4 extend toward a threefold symmetry axis of the capsid in the native virion, whereas the same residues point toward a twofold symmetry axis in the rhinovirus 14–ICAM-1 complex (Fig. 5*A*). The movement of the C terminus of VP4 is induced by conformational changes of the major capsid proteins, which are triggered by ICAM-1 binding to the capsid. In the rhinovirus-14 virion, the C-terminal carboxyl group of Asn68 from VP4 forms a salt bridge with the side chain of Arg12 of VP2 (Fig. 5 *C* and *E*). Additionally, the side chain of Asn68 forms two hydrogen bonds with the side chain of Asp11 of VP2 (Fig. 5 *C* and *E*). As discussed above, the binding of ICAM-1 to rhinovirus 14 induces a rotation of VP1 toward VP2 and VP3 (Fig. 4*A*). These movements of capsid proteins bring residues 27 to 33 from the N terminus of VP2 into the space that is occupied by Arg12 of VP2 in the native virion (Fig. 5 *D* and *F*). This frees the C terminus of VP4 from the interaction with Arg12 of VP2 and probably enables its translocation toward a twofold axis (Fig. 5 *A*, *D*, and *F*). The restructuring of the C-terminal part of VP4 to point toward a twofold symmetry axis prepares the protein for release through either of the holes that form at and next to the twofold symmetry axes upon particle activation (Fig. 5 *A* and *B*) (29, 34).

**ICAM-1 Binding Induces Changes in Genome Organization of Rhinovirus 14.** The binding of ICAM-1 into the canyon of rhinovirus 14 induces the relocation of the C terminus of VP4 toward a twofold symmetry axis of the capsid (Fig. 5*A*). The movement of the C terminus of VP4 uncovers a patch of positively charged residues at the inner face of the capsid, adjacent to a threefold symmetry axis (Fig. 6 *A* and *B*). The positively charged surface attracts genomic RNA, which is represented in the cryo-EM reconstruction as a cylindrical appendage emanating from the spherical genome density filling the center of the virus particle (Fig. 6 *C–F*). This indicates that parts of the RNA genome in various conformations interact nonspecifically with the positively charged regions of the capsid. Furthermore, the N termini of VP2 subunits probably interact with the RNA density positioned on a threefold axis (Fig. 6*F*). The C terminus of VP4 positioned next to a twofold axis of the capsid covers the side chain of Trp38 of VP2, which in the native virion forms a stacking interaction with a nucleotide from the RNA genome (Figs. 1*D* and 5 *E* and *F* and *SI Appendix*, Fig.

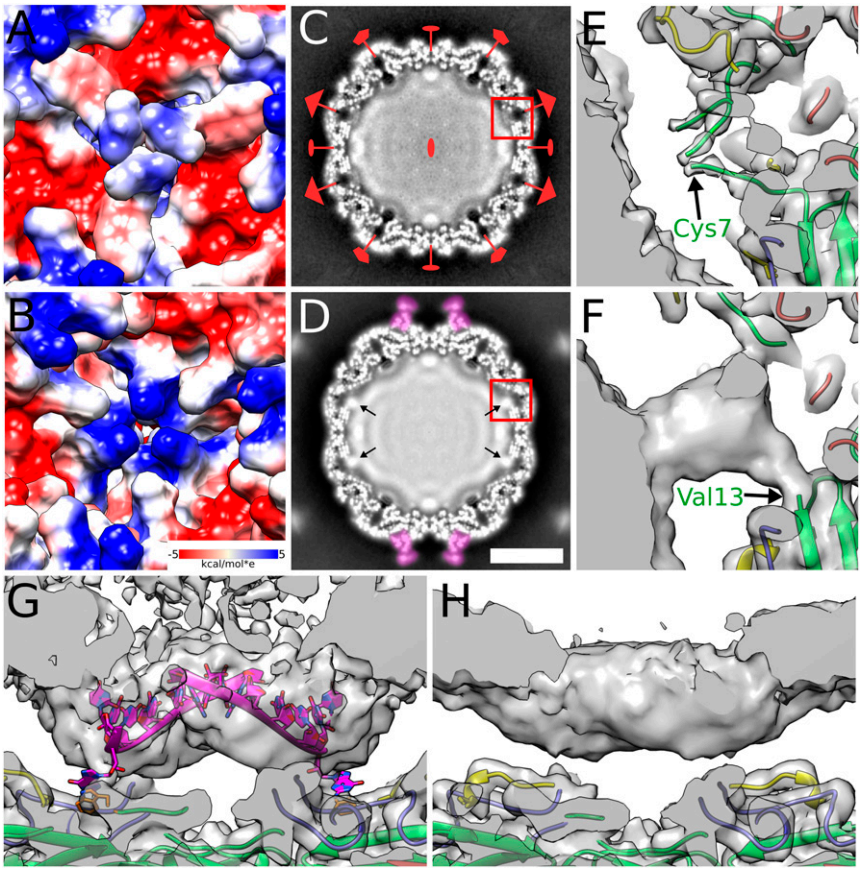


**Fig. 6.** Conformational changes of capsid of rhinovirus 14 that are induced by binding to ICAM-1 trigger redistribution of RNA genome in the particle. (*A* and *B*) Detail of inner capsid surface around threefold symmetry axis of virion (*A*) and rhinovirus 14–ICAM-1 complex (*B*). The surfaces are colored according to charge. (*C* and *D*) Electron densities of central slices of cryo-EM reconstructions of virion (*C*) and rhinovirus 14–ICAM-1 complex (*D*) with a thickness of 1 Å. White represents high density values. Density representing ICAM-1 is highlighted in magenta. Positions of icosahedral symmetry axes are indicated with an oval, triangle, and pentagon for twofold, threefold, and fivefold axes, respectively. Black arrows in *D* point toward densities on threefold symmetry axes, which are not present in the virion. Red squares indicate positions of details shown at higher magnification in *E* and *F*. (Scale bar, 10 nm.) (*E* and *F*) Details of cryo-EM density distribution at the inner face of the capsid on a threefold symmetry axis. Capsid proteins are shown in cartoon representation with VP1 in blue, VP2 in green, VP3 in red, and VP4 in yellow. Cryo-EM density is shown as a semitransparent gray surface. Positions of the first resolved residues from the N termini of VP2 subunits are indicated. *E* and *F* show sections of particles with a thickness of 20 Å. (*G* and *H*) Comparison of structures of RNA genome interacting with VP2 subunits in virion (*G*) and rhinovirus 14–ICAM-1 complex (*H*). The virion contains resolved cryo-EM density corresponding to octanucleotides (*G*). In contrast, there is a featureless density in the rhinovirus 14–ICAM-1 complex (*H*). Capsid proteins are shown in cartoon representation, colored as in *E* and *F*.

S2). The loss of Trp38–RNA contact relaxes the ordering of segments of the RNA genome that interact with the capsid around twofold symmetry axes in native virions (Fig. 6 *G* and *H*). A density corresponding to RNA at the twofold axis in the rhinovirus 14–ICAM-1 complex does not have resolved features (Fig. 6 *G* and *H*). The interactions of the N termini of VP1 subunits with the RNA genome remain preserved even after the binding of rhinovirus 14 to ICAM-1 (Fig. 1*E*). The binding of rhinovirus 14 to ICAM-1 induces a rearrangement of the RNA genome, which may play a role in particle activation, as discussed below.

**Binding of ICAM-1 Primes Particles of Rhinovirus 14 for Activation and Genome Release.** The binding of ICAM-1 to rhinovirus 14 triggers a cascade of structural changes that prepare the particle for activation and subsequent genome release (Fig. 7 *A* and *B*). The rotation of VP1 subunits results in a narrowing of the canyon and transmits the conformational changes to the inside of the capsid (Fig. 7 *C* and *D*). C termini of VP4 subunits reposition toward twofold symmetry axes, where they are optimally poised for externalization upon particle activation (Fig. 7 *E* and *F*). The conformational change to C termini of VP4 subunits uncovers patches of positively charged residues that attract genomic RNA toward threefold symmetry axes of the capsid (Fig. 7 *G* and *H*). The same conformational change prevents the interaction of Trp38 from VP2 with bases from the ordered RNA segments of the genome positioned next to twofold symmetry axes of the capsid (Fig. 7 *G* and *H*). Both of these effects result in reorganization of the RNA genome (Fig. 7 *G* and *H*). These changes in the capsid and genome structure of rhinovirus 14 induced by ICAM-1 binding are required for efficient genome release at acidic pH (Fig. 2). All in all, 90% of virions of rhinovirus 14 exposed to pH 6.2 remained in their native conformation, whereas the remaining particles were empty (Fig. 2 *A*, *B*, *E*, and *F* and *SI Appendix*, Table S1). The structures of rhinovirus 14 in their native conformation and empty capsids at acidic pH were determined to resolutions of 2.8 and 3.9 Å, respectively (Fig. 2 *A* and *B* and *SI Appendix*, Table S1). The exposure of rhinovirus 14 to acidic pH did not induce structural changes in VP4 subunits (Fig. 2 *E* and *F*). In contrast, the exposure of rhinovirus 14–ICAM-1 complex to pH 6.2 resulted in activation and genome release from 95% of particles (Fig. 2 *C*, *D*, *E*, and *H*). The structure of the activated particle was determined to a resolution of 4.0 Å, empty particle to 3.9 Å, and open particle to 22 Å

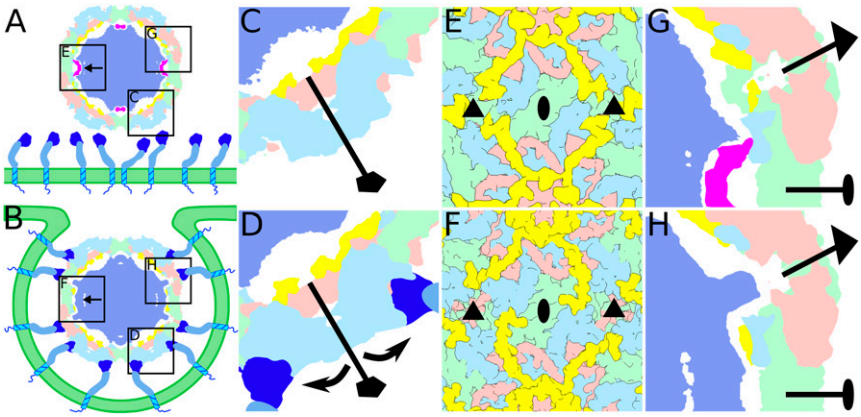


**Fig. 7.** Overview of structural changes to rhinovirus 14 induced by binding of ICAM-1 that prepare the virus for activation and genome release. (*A*) Native virion diffuses toward cell membrane (green ribbon) decorated with ICAM-1 molecules (blue sticks with dark blue heads representing domain 1). The virus particle is represented by a central slice with the electron density of VP1 shown in light blue, VP2 in light green, VP3 in light red, VP4 in yellow, the genome in purple, and resolved RNA segments in pink. (*B*) Rhinovirus 14 is endocytosed by the cell after binding to ICAM-1. (*C–H*) Sequence of structural changes in virion induced by binding to ICAM-1. *C*, *E*, and *G* represent native virion, whereas *D*, *F*, and *H* show rhinovirus 14–ICAM-1 complex. (*C* and *D*) Binding of ICAM-1 induces rotation of VP1 subunit toward VP2 and VP3. Virus components are colored as in *A*. (*E* and *F*) ICAM-1 binding induces disruption of interactions between C terminus of VP4 and N terminus of VP2. C terminus of VP4 repositions from a threefold symmetry axis (indicated with a triangle) toward a twofold symmetry axis (oval). (*G* and *H*) Movements of C termini of VP4 subunits uncover positively charged residues around twofold symmetry axes, which attract negatively charged RNA genome. Furthermore, the C terminus of VP4 in the altered conformation covers Trp38 of VP2 and prevents its specific interaction with structured segments of the RNA genome, which relaxes the structure of RNA adjacent to the twofold symmetry axis.

(Fig. 2 *C* and *D* and *SI Appendix*, Table S1). The changes in the capsid and genome of rhinovirus 14, which were induced by ICAM-1 binding, may lower the energy barrier of particle activation so that it can be overcome by random fluctuations in particle structure due to thermal motions termed "capsid breathing" (58, 59). This provides a putative explanation of how the reduction of capsid dynamics by antiviral compounds, which target VP1 pockets (59), blocks the activation and genome release of enteroviruses.

The sample of complex of rhinovirus 14 with ICAM-1 exposed to acidic pH contained 7% empty particles missing a pentamer of capsid protein protomers (Fig. 2*D*). Open particles were previously speculated to enable enterovirus genome release (33). The expulsion of pentamers of capsid proteins results in the formation of a large hole in the capsid, which enables the diffusion of the RNA genome from the capsid within a microsecond (33, 60). The rapid release of a genome may be connected to its subsequent transport across the endosome membrane into the cytoplasm (61, 62).

Structural characterization of the rhinovirus 14–ICAM-1 complex at atomic resolution provides detailed information about the conformational changes of both the receptor and virus that are required for its binding. Additionally, it provides insight into the structural changes of the virus that enable subsequent particle activation and genome release. In combination, these results provide the basis for the design of compounds that block enterovirus infection.

## Materials and Methods

**Expression and Purification of ICAM-1 D1 to D5.** The extracellular part of ICAM-1 containing domains D1 to D5 was produced using the MutiBac system (Geneva Biotech). The full-length gene of ICAM-1 was a gift from Timothy Springer (Harvard Medical School, Boston, MA) (Addgene plasmid No. 8632; http://addgene.org/8632; RRID: Addgene 8632). The sequence encoding domains D1 to D5, the secretion signal peptide, and the C-terminal 10 His-tag were inserted into the pACEBac1 vector at the restriction site BamHI. The recombinant bacmid with the target sequence was prepared by recombination in DH10EMBacY *Escherichia coli* cells (Geneva Biotech). The recombinant baculovirus was prepared by transfecting *SF9* cells with the recombinant bacmid. A total of 250 mL of the culture of *SF9* cells were infected with the recombinant baculovirus and incubated for 96 h at 27 °C with 120 rpm shaking. The produced protein was secreted into the medium. Cells and cell debris were pelleted by centrifugation at 20,000 × *g* at 4 °C for 15 min. The supernatant was filtered through a 0.2 μm filter (Corning) and loaded into a HisTrap column (GE Healthcare) equilibrated in PBS (137 mM NaCl, 2.7 mM KCl, 10 mM $Na_2HPO_4$, 1.8 mM $KH_2PO_4$, pH 7.4). Most of the impurities were removed by washing with PBS containing 70 mM imidazole. His-tagged ICAM-1 D1 to D5 was eluted using PBS with 500 mM imidazole. The eluted protein was buffer exchanged into PBS using 30 kDa cutoff centrifugal concentrators (Millipore, Merck). The target protein was further purified by size-exclusion chromatography, using a HiLoad 16/600 Superdex 200 pg column (GE Healthcare). Fractions containing ICAM-1 D1 to D5 were pooled and concentrated using centrifugal concentrators (Millipore, Merck) to a final concentration of 3.5 mg/mL.

**Rhinovirus 14 Purification.** Rhinovirus-14 strain 1059, obtained from ATCC, was propagated in HeLa-H1 (ATCC CRL195) cells cultivated in Dulbecco's modified Eagle's medium enriched with 10% fetal bovine serum. HeLa cells grown to 100% confluence (100 tissue culture dishes, 150 mm diameter) were infected with a multiplicity of infection of 0.1. The infection was allowed to progress for 36 h until a complete cytopathic effect was observed. The media and cells were harvested and centrifuged at 15,000 × *g* at 10 °C for 30 min. The resulting pellet was subjected to three freeze–thaw cycles and resuspended in 5 mL PBS followed by homogenization in a Dounce tissue grinder. Cell debris was separated from the supernatant by centrifugation at 4,000 × *g* for 30 min at 10 °C. The virus-containing supernatant was combined with the media from infected cells. The virus particles were precipitated by the addition of PEG-8000 and NaCl to final concentrations of 12.5% (wt/vol) and 500 mM, respectively, and incubation overnight at 10 °C. The precipitated virus was pelleted by centrifugation at 15,000 × *g* at 10 °C for 30 min. The pellet was resuspended in 20 mL PBS with 5 nm $MgCl_2$. The sample was subjected to DNase (10 μg/mL final concentration) and RNase (10 μg/mL final concentration) treatment at room temperature for 30 min. Subsequently, trypsin was added to a final concentration of 0.5 μg/mL, and the sample was incubated at 37 °C for 15 min. EDTA (pH = 9.5) and Nonidet P-40 (Sigma-Aldrich) were added to final concentrations of 15 mM and 1% (vol/vol), respectively. The virus was pelleted through a 30% (wt/vol) sucrose cushion by centrifugation at 210,000 × *g* in an Optima ×80 ultracentrifuge (Beckman Coulter) using a Ti50.2 rotor. The pelleted virus particles were resuspended in 2 mL PBS, loaded on the top of a 60% (wt/wt) CsCl solution in PBS, and centrifuged at 160,000 × *g* in an Optima ×80 ultracentrifuge using a Beckman Coulter SW41Ti rotor at 10 °C for 24 h. Opaque bands containing virus particles were harvested and subjected to buffer exchange in PBS using a Centricon Plus-70 centrifugal filter (Millipore) with a 100 kDa cutoff. The final concentration of rhinovirus 14 was 0.5 mg/mL. Purified virus was kept at 4 °C.

**Preparation of Rhinovirus 14–ICAM-1 Complex and Exposure to Acidic pH.** The complex of rhinovirus 14 with ICAM-1 was prepared by mixing rhinovirus 14 with ICAM-1 at a molar ratio of 1:100 at pH 7.4 and incubating the mixture

for 30 min at 34 °C. Rhinovirus 14 and the rhinovirus 14–ICAM-1 complex were transferred to acidic pH using DyeEx 2.0 (QIAGEN) spin columns containing PBS with pH 6.2. The samples were applied onto the columns and eluted by 1 min of centrifugation at 1,200 × *g*. The samples were incubated at pH 6.2 at 34 °C for 2.5 min, including the centrifugation step.

**Cryo-EM Sample Preparation and Data Collection.** For vitrification, 3 μL virus samples were applied onto a holey carbon-coated copper grid (R2/1, mesh 300, Quantifoil), blotted for 2 s, and vitrified by plunging into liquid ethane using a Vitrobot Mark IV (Thermo Fisher Scientific). Grids for virion reconstruction were prepared by vitrifying a virus sample with a concentration of 0.5 mg/mL. The grids (except for those with rhinovirus 14 at pH 6.2) were then transferred to a Titan Krios electron microscope, operating at 300 kV at cryogenic conditions, equipped with a Falcon III direct electron detector (Thermo Fisher Scientific). The illuminating beam was aligned for parallel illumination in NanoProbe mode. Low-dose imaging was used with a total dose of 84.7 $e^-/Å^2$. Nominal magnification was set to 75,000×, resulting in a calibrated pixel size of 1.063 Å. The dataset was recorded automatically using EPU software (Thermo Fisher Scientific) in fast acquisition mode, using large image shifts. The samples of rhinovirus 14 and rhinovirus 14–ICAM-1 complex were recorded using five acquisitions per hole, nine holes per stage shift. The sample of rhinovirus 14–ICAM-1 complex at pH 6.2 was recorded using seven acquisitions per hole, nine holes per stage shift. The exposure time was set to 1 s, and each micrograph was recorded as a movie containing 40 frames. The target defocus range was −0.5 to −2.4 μm.

Electron micrographs from the sample of rhinovirus 14 at pH 6.2 were collected using a Talos Arctica electron microscope (Thermo Fisher Scientific), operated at 200 kV under cryogenic conditions, equipped with a Falcon III direct electron detector (Thermo Fisher Scientific). The illuminating beam was aligned for parallel illumination in NanoProbe mode. Low-dose imaging was used with a total dose of 34.1 $e^-/Å^2$. Nominal magnification was set to 120,000×, resulting in a calibrated pixel size of 1.22 Å. The dataset was recorded automatically using EPU software (Thermo Fisher Scientific) in fast acquisition mode, using five acquisitions per hole, nine holes per stage shift. The exposure time was set to 1 s, and each micrograph was recorded as a movie containing 40 frames. The target defocus range was −0.5 to −2.4 μm.

**Image Processing.** The beam-induced movements within one micrograph were corrected with the software MotionCorr2 using 5 × 5 patches (63). The motion-corrected micrographs were dose weighted, and defocus values were estimated using the program gCTF (64). Using crYOLO box manager (65), 200 particles were boxed manually and used as a template for ab initio model training. The resulting crYOLO model was used to pick particles. The particles were extracted using Relion3.1 (66) with a box size of 546 px. The particles were binned to a box size of 150 × 150 px and subjected to reference-free two-dimensional classifications in Relion3.1 (66). Particles from classes exhibiting high-resolution features were used for de novo model calculation with imposed icosahedral symmetry, using stochastic gradient descent as implemented in Relion3.1 (66). The resulting three-dimensional (3D) volume was used as a starting model for autorefinement in Relion3.1. After initial autorefinement, 3D classification in Relion3.1 was performed, omitting the alignment step. Particles belonging to the best class were reextracted and recentered box-size 512 × 512 px for rhinovirus 14 particles without ICAM-1 and 546 × 546 px for the rhinovirus 14–ICAM-1 complex. Reextracted particles were subjected to another round of autorefinement in Relion3.1. Particles were then sorted into nine optic groups. The optics groups were determined by the position of the image shift used for the acquisition, whereas all the acquisition areas from the same foil hole were considered as one optics group. Therefore, only large (interhole) image shifts were considered as separate optics groups. Magnification correction was performed using Relion3.1, followed by beam-tilt correction, and subsequently by the estimation of third- and fourth-order Zernike polynomials. The aberration-corrected particles were further subjected to per-particle defocus and astigmatism correction and estimation of the CTF envelope function (CTF B-factor fitting). The particles were subjected to autorefinement with imposed icosahedral symmetry. Ewald sphere correction was performed as implemented in relion_reconstruct.py in Relion3.1 (67). The resulting map was used for Bayesian polishing of particles with default parameters. The polished particles were used for 3D autorefinement and CTF refinement followed by another 3D autorefinement. Finally, Ewald sphere correction was performed. The final map was threshold masked, divided by a modulation transfer function, and B-factor sharpened using Relion3.1. Local resolutions were estimated using the program MonoRes implemented in the Scipion software package (68, 69). Map B-factor sharpening based on local resolution estimation from MonoRes was performed using the program LocalDeblur (70). The dataset of rhinovirus 14 with ICAM-1 exposed to pH 6.2 contained empty capsids missing pentamers. These were identified by 3D classification with C5 symmetry, using the complete empty capsid as an initial model. Subsequent 3D autorefinement was performed with C5 symmetry. Neither CTF refinement nor Bayesian polishing were applied to this subset of particles.

**Building and Refinement of Atomic Structure.** The electrostatic potential map from cryo-EM reconstruction was oriented to the standard 222 icosahedral crystallographic orientation. The origin of the map was moved from the 0,0,0, coordinate to the center of the particle using the program mapman (71). The map was normalized and converted to crystallographic space group P23 using the CCP4i software suite (72). The higher-symmetry space group was used to reduce the computational demands of the model refinement. Crystal structures of rhinovirus 14 (Protein Data Bank [PDB]: 4RHV) and domain 1 of ICAM-1 (PDB: 1IC1) were manually fitted into the cryo-EM maps using the program Chimera and refined with the tool "Fit in map" (73). The cryo-EM structure of an empty particle of rhinovirus 14 in complex with a Fab fragment of antibody (PDB: 5W3O) was used as a starting model for the building of activated and empty particles (74). The fitted models were subjected to multiple rounds of real-space refinement in Phenix (version dev-3765), reciprocal-space refinement in REFMAC5, combined with manual corrections in Coot 0.9 and ISOLDE (75–78). Hydrogen atoms were taken into account during the real-space refinement, whereas they were ignored in the reciprocal-space refinement. Waters were added automatically by the program "find waters" in Coot 0.9 and validated manually. Model validation parameters were calculated using MolProbity server and EMringer as implemented in phenix (79, 80). The RNA octanucleotide sequence in the native virion of rhinovirus 14 was initially built using the program Coot and refined with restraints using the program ISOLDE (78). Structural comparisons were performed in Chimera (73). Hydrogen bonds, salt bridges, and residues involved in the binding interface and buried surface areas were calculated using the program PDBePISA (https://www.ebi.ac.uk/pdbe/pisa/). Roadmaps were produced using the program Rivem (81).

**Mass Spectrometry Analyses.** Purified samples of ICAM-1 and the complex of rhinovirus 14 with ICAM-1 were digested with alpha-lytic protease (EC 3.4.21.12, Sigma-Aldrich catalog No. A6362) for 2 h at 37 °C with shaking at 700 rpm. Half of the volume of each sample was then reduced using 10 mM DTT (for 45 min at 57 °C with shaking at 700 rpm). After adding polyethylene glycol to a final concentration of 0.001%, the peptides were extracted from the vials using 25% formic acid/acetonitrile (1:1 vol/vol mixture) and vacuum concentrated. The peptide mixture was subjected to liquid-chromatography-mass spectrometry (LC-MS)/MS analysis using a RSLCnano system (ThermoFisher Scientific) coupled to an Impact II Qq-Time-Of-Flight mass spectrometer (Bruker). Prior to LC separation, peptides were online concentrated in a trap column (100 μm × 30 mm) filled with 3.5 μm X-Bridge BEH 130 C18 sorbent (Waters). The peptides were separated using an Acclaim Pepmap100 C18 column (3 μm particles, 75 μm × 500 mm; ThermoFisher Scientific) by the following LC gradient program (mobile phase A: 0.1% formic acid in water; mobile phase B: 0.1% formic acid in 80% acetonitrile; 300 nl/min): the gradient elution started at 1% of mobile phase B and increased to 56% over the first 50 min, then increased linearly to 80% of mobile phase B over the next 5 min and remained at this state for the final 10 min. Equilibration of the trapping column and the column was done prior to sample injection into the sample loop. The analytical column outlet was directly connected to a CaptiveSpray nanoBooster ion source (Bruker). The nanoBooster was filled with acetonitrile. MS and MS/MS spectra were acquired in a data-dependent strategy with a 3 s cycle time. The mass range was set to 150 to 2,200 m/z and precursors were selected from 300 to 2,000 m/z. The acquisition speed of MS and MS/MS scans was 2 Hz and 4 to 16 Hz, respectively. The speed of MS/MS spectra acquisition was based on precursor intensity. The preprocessing of the mass spectrometric data including recalibration, compound detection, and charge deconvolution was carried out using DataAnalysis software (version 4.2 SR1; Bruker).

The obtained data were searched with an in-house Mascot search engine (version 2.4.1; Matrixscience) against a custom database involving the ICAM-1 sequence and cRAP entries (downloaded from https://www.thegpm.org/crap/). The database searches were done without enzyme specificity and with oxidation (M) as a variable modification. The mass tolerances for peptides and MS/MS fragments were 10 ppm and 0.1 Da, respectively. Only peptides with a statistically significant peptide score ($P < 0.05$) were considered, and the obtained MS/MS data were validated manually.

**Multiple Sequence Alignment.** Multiple sequence alignment of capsid proteins of selected viruses from the family *Picornaviridae* was performed in the Clustal Omega server (82). The multiple sequence alignment was visualized in the software Jalview 2.11.1.3 (83).

**Data Availability.** The cryo-EM maps and coordinates were deposited under the following accession codes: virion of rhinovirus 14 at neutral pH Electron Microscopy Data Bank EMD-12171 and PDB 7BG6; rhinovirus 14–ICAM-1 complex at neutral pH EMD-12172 and PDB 7BG7; rhinovirus 14 in native conformation at acidic pH EMD-12599 and PDB 7NUQ; empty particle of rhinovirus 14 at acidic pH EMD-12597 and PDB 7NUO; rhinovirus 14 in native conformation at acidic pH originating from complex with ICAM-1 EMD-12596 and PDB 7NUN; activated particle originating from complex with ICAM-1 at acidic pH EMD-12594 and PDB 7NUL; empty particle originating from complex with ICAM-1 at acidic pH EMD-12595 and PDB 7NUM; and open particle originating from complex with ICAM-1 at acidic pH EMD-12598.

**ACKNOWLEDGMENTS.** We gratefully acknowledge the Cryo-Electron Microscopy and Tomography Core Facility of Central European Institute of Technology (CEITEC) supported by Ministry of Education, Youth, and Sports of the Czech Republic (MEYS CR) (Grant LM2018127). This research was carried out under the project CEITEC 2020 (Grant LQ1601), with financial support from the MEYS of the Czech Republic under National Sustainability Program II. This work was supported by the IT4I project (Grant CZ.1.05/1.1.00/02.0070) and funded by the European Regional Development Fund and the national budget of the Czech Republic via the Research and Development for Innovations Operational Programme (RDI-OP) as well as the MEYS via Grant LM2011033. The research leading to these results received funding from Czech Science Foundation Grant GX19-25982X to P.P.

1. S. E. Jacobs, D. M. Lamson, K. St George, T. J. Walsh, Human rhinoviruses. *Clin. Microbiol. Rev.* **26**, 135–162 (2013).
2. A. M. Fendrick, A. S. Monto, B. Nightengale, M. Sarnes, The economic burden of non-influenza-related viral respiratory tract infection in the United States. *Arch. Intern. Med.* **163**, 487–494 (2003).
3. J. S. Bertino, Cost burden of viral respiratory infections: Issues for formulary decision makers. *Am. J. Med.* **112** (suppl. 6A), 42S–49S (2002).
4. A. C. Palmenberg *et al*., Sequencing and analyses of all known human rhinovirus genomes reveal structure and evolution. *Science* **324**, 55–59 (2009).
5. J. M. Greve *et al*., The major human rhinovirus receptor is ICAM-1. *Cell* **56**, 839–847 (1989).
6. C. R. Uncapher, C. M. DeWitt, R. J. Colonno, The major and minor group receptor families contain all but one human rhinovirus serotype. *Virology* **180**, 814–817 (1991).
7. F. Hofer *et al*., Members of the low density lipoprotein receptor family mediate cell entry of a minor-group common cold virus. *Proc. Natl. Acad. Sci. U.S.A.* **91**, 1839–1842 (1994).
8. Y. A. Bochkov *et al*., Cadherin-related family member 3, a childhood asthma susceptibility gene product, mediates rhinovirus C binding and replication. *Proc. Natl. Acad. Sci. U.S.A.* **112**, 5485–5490 (2015).
9. A. I. Wells, C. B. Coyne, Enteroviruses: A gut-wrenching game of entry, detection, and evasion. *Viruses* **11**, 460 (2019).
10. J. M. Bergelson *et al*., Decay-accelerating factor (CD55), a glycosylphosphatidylinositol-anchored complement regulatory protein, is a receptor for several echoviruses. *Proc. Natl. Acad. Sci. U.S.A.* **91**, 6245–6248 (1994).
11. Y. Nishimura *et al*., Human P-selectin glycoprotein ligand-1 is a functional receptor for enterovirus 71. *Nat. Med.* **15**, 794–797 (2009).
12. J. Staring *et al*., KREMEN1 is a host entry receptor for a major group of enteroviruses. *Cell Host Microbe* **23**, 636–643.e5 (2018).
13. P. Y. Su *et al*., Cell surface sialylation affects binding of enterovirus 71 to rhabdomyosarcoma and neuroblastoma cells. *BMC Microbiol.* **12**, 162 (2012).
14. C. L. Mendelsohn, E. Wimmer, V. R. Racaniello, Cellular receptor for poliovirus: Molecular cloning, nucleotide sequence, and expression of a new member of the immunoglobulin superfamily. *Cell* **56**, 855–865 (1989).
15. J. M. Bergelson *et al*., Isolation of a common receptor for Coxsackie B viruses and adenoviruses 2 and 5. *Science* **275**, 1320–1323 (1997).
16. S. Yamayoshi *et al*., Scavenger receptor B2 is a cellular receptor for enterovirus 71. *Nat. Med.* **15**, 798–801 (2009).
17. T. J. Tuthill, E. Groppelli, J. M. Hogle, D. J. Rowlands, Picornaviruses. *Curr. Top. Microbiol. Immunol.* **343**, 43–89 (2010).
18. R. Basavappa *et al*., Role and mechanism of the maturation cleavage of VP0 in poliovirus assembly: Structure of the empty capsid assembly intermediate at 2.9 A resolution. *Protein Sci.* **3**, 1651–1669 (1994).
19. J. J. Holland, E. D. Kiehn, Specific cleavage of viral proteins as steps in the synthesis and maturation of enteroviruses. *Proc. Natl. Acad. Sci. U.S.A.* **60**, 1015–1022 (1968).
20. M. Procházková *et al*., Virion structures and genome delivery of honeybee viruses. *Curr. Opin. Virol.* **45**, 17–24 (2020).
21. M. G. Rossmann *et al*., Structure of a human common cold virus and functional relationship to other picornaviruses. *Nature* **317**, 145–153 (1985).
22. S. C. Harrison, A. J. Olson, C. E. Schutt, F. K. Winkler, G. Bricogne, Tomato bushy stunt virus at 2.9 A resolution. *Nature* **276**, 368–373 (1978).
23. N. Verdaguer, D. Blaas, I. Fita, Structure of human rhinovirus serotype 2 (HRV2). *J. Mol. Biol.* **300**, 1179–1194 (2000).
24. M. A. Oliveira *et al*., The structure of human rhinovirus 16. *Structure* **1**, 51–68 (1993).
25. M. Smyth, T. Pettitt, A. Symonds, J. Martin, Identification of the pocket factors in a picornavirus. *Arch. Virol.* **148**, 1225–1233 (2003).
26. A. Pickl-Herk *et al*., Uncoating of common cold virus is preceded by RNA switching as determined by X-ray and cryo-EM analyses of the subviral A-particle. *Proc. Natl. Acad. Sci. U.S.A.* **110**, 20063–20068 (2013).
27. H. C. Levy, M. Bostina, D. J. Filman, J. M. Hogle, Catching a virus in the act of RNA release: A novel poliovirus uncoating intermediate characterized by cryo-electron microscopy. *J. Virol.* **84**, 4426–4441 (2010).
28. D. Garriga *et al*., Insights into minor group rhinovirus uncoating: The X-ray structure of the HRV2 empty capsid. *PLoS Pathog.* **8**, e1002473 (2012).
29. X. Wang *et al*., A sensor-adaptor mechanism for enterovirus uncoating from structures of EV71. *Nat. Struct. Mol. Biol.* **19**, 424–429 (2012).
30. K. L. Shingler *et al*., The enterovirus 71 A-particle forms a gateway to allow genome release: A cryoEM study of picornavirus uncoating. *PLoS Pathog.* **9**, e1003240 (2013).
31. J. J. Seitsonen *et al*., Structural analysis of coxsackievirus A7 reveals conformational changes associated with uncoating. *J. Virol.* **86**, 7207–7215 (2012).
32. D. M. Belnap *et al*., Molecular tectonic model of virus structural transitions: The putative cell entry states of poliovirus. *J. Virol.* **74**, 1342–1354 (2000).
33. D. Buchta *et al*., Enterovirus particles expel capsid pentamers to enable genome release. *Nat. Commun.* **10**, 1138 (2019).
34. J. Ren *et al*., Picornavirus uncoating intermediate captured in atomic detail. *Nat. Commun.* **4**, 1929 (2013).
35. L. Bauer, H. Lyoo, H. M. van der Schaar, J. R. Strating, F. J. van Kuppeveld, Direct-acting antivirals and host-targeting strategies to combat enterovirus infections. *Curr. Opin. Virol.* **24**, 1–8 (2017).
36. T. J. Smith *et al*., The site of attachment in human rhinovirus 14 for antiviral agents that inhibit uncoating. *Science* **233**, 1286–1293 (1986).
37. A. van de Stolpe, P. T. van der Saag, Intercellular adhesion molecule-1. *J. Mol. Med. (Berl.)* **74**, 13–33 (1996).
38. J. M. Casasnovas, T. Stehle, J. H. Liu, J. H. Wang, T. A. Springer, A dimeric crystal structure for the N-terminal two domains of intercellular adhesion molecule-1. *Proc. Natl. Acad. Sci. U.S.A.* **95**, 4134–4139 (1998).
39. C. Chothia, E. Y. Jones, The molecular structure of cell adhesion molecules. *Annu. Rev. Biochem.* **66**, 823–862 (1997).
40. J. Wang, T. A. Springer, Structural specializations of immunoglobulin superfamily members for adhesion to integrins and viruses. *Immunol. Rev.* **163**, 197–215 (1998).
41. Y. Harpaz, C. Chothia, Many of the immunoglobulin superfamily domains in cell adhesion molecules and surface receptors belong to a new structural set which is close to that containing variable domains. *J. Mol. Biol.* **238**, 528–539 (1994).
42. P. R. Kolatkar *et al*., Structural studies of two rhinovirus serotypes complexed with fragments of their cellular receptor. *EMBO J.* **18**, 6249–6259 (1999).
43. C. Xiao *et al*., Discrimination among rhinovirus serotypes for a variant ICAM-1 receptor molecule. *J. Virol.* **78**, 10034–10044 (2004).
44. C. Xiao *et al*., Interaction of coxsackievirus A21 with its cellular receptor, ICAM-1. *J. Virol.* **75**, 2444–2451 (2001).
45. N. H. Olson *et al*., Structure of a human rhinovirus complexed with its receptor molecule. *Proc. Natl. Acad. Sci. U.S.A.* **90**, 507–511 (1993).
46. L. Xing, J. M. Casasnovas, R. H. Cheng, Structural analysis of human rhinovirus complexed with ICAM-1 reveals the dynamics of receptor-mediated virus uncoating. *J. Virol.* **77**, 6101–6107 (2003).
47. H. Hoover-Litty, J. M. Greve, Formation of rhinovirus-soluble ICAM-1 complexes and conformational changes in the virion. *J. Virol.* **67**, 390–397 (1993).
48. J. M. Hogle, M. Chow, D. J. Filman, Three-dimensional structure of poliovirus at 2.9 A resolution. *Science* **229**, 1358–1365 (1985).
49. J. K. Muckelbauer *et al*., Structure determination of coxsackievirus B3 to 3.5 A resolution. *Acta Crystallogr. D Biol. Crystallogr.* **51**, 871–887 (1995).
50. E. Hendry *et al*., The crystal structure of coxsackievirus A9: New insights into the uncoating mechanisms of enteroviruses. *Structure* **7**, 1527–1538 (1999).
51. C. Xiao *et al*., The crystal structure of coxsackievirus A21 and its interaction with ICAM-1. *Structure* **13**, 1019–1033 (2005).
52. E. R. McFadden Jr. *et al*., Thermal mapping of the airways in humans. *J. Appl. Physiol.* **58**, 564–570 (1985).
53. L. Xing *et al*., Distinct cellular receptor interactions in poliovirus and rhinoviruses. *EMBO J.* **19**, 1207–1216 (2000).
54. A. McClelland *et al*., Identification of monoclonal antibody epitopes and critical residues for rhinovirus binding in domain 1 of intercellular adhesion molecule 1. *Proc. Natl. Acad. Sci. U.S.A.* **88**, 7993–7997 (1991).
55. M. A. Sun *et al*., Prediction of reversible disulfide based on features from local structural signatures. *BMC Genomics* **18**, 279 (2017).
56. R. B. Register, C. R. Uncapher, A. M. Naylor, D. W. Lineberger, R. J. Colonno, Human-murine chimeras of ICAM-1 identify amino acid residues critical for rhinovirus and antibody binding. *J. Virol.* **65**, 6589–6596 (1991).
57. N. Verdaguer, I. Fita, M. Reithmayer, R. Moser, D. Blaas, X-ray structure of a minor group human rhinovirus bound to a fragment of its cellular receptor protein. *Nat. Struct. Mol. Biol.* **11**, 429–434 (2004).
58. Q. Li, A. G. Yafal, Y. M. Lee, J. Hogle, M. Chow, Poliovirus neutralization by antibodies to internal epitopes of VP4 and VP1 results from reversible exposure of these sequences at physiological temperature. *J. Virol.* **68**, 3965–3970 (1994).
59. J. K. Lewis, B. Bothner, T. J. Smith, G. Siuzdak, Antiviral agent blocks breathing of the common cold virus. *Proc. Natl. Acad. Sci. U.S.A.* **95**, 6774–6778 (1998).
60. K. Škubník *et al*., Capsid opening enables genome release of iflaviruses. *Sci. Adv.* **7**, eabd7130 (2021).
61. M. Bostina, H. Levy, D. J. Filman, J. M. Hogle, Poliovirus RNA is released from the capsid near a twofold symmetry axis. *J. Virol.* **85**, 776–783 (2011).

MICROBIOLOGY

62. M. Strauss, H. C. Levy, M. Bostina, D. J. Filman, J. M. Hogle, RNA transfer from poliovirus 135S particles across membranes is mediated by long umbilical connectors. *J. Virol.* **87**, 3903–3914 (2013).
63. S. Q. Zheng *et al*., MotionCor2: Anisotropic correction of beam-induced motion for improved cryo-electron microscopy. *Nat. Methods* **14**, 331–332 (2017).
64. K. Zhang, Gctf: Real-time CTF determination and correction. *J. Struct. Biol.* **193**, 1–12 (2016).
65. T. Wagner *et al*., SPHIRE-crYOLO is a fast and accurate fully automated particle picker for cryo-EM. *Commun. Biol.* **2**, 218 (2019).
66. S. H. Scheres, A Bayesian view on cryo-EM structure determination. *J. Mol. Biol.* **415**, 406–418 (2012).
67. C. J. Russo, R. Henderson, Ewald sphere correction using a single side-band image processing algorithm. *Ultramicroscopy* **187**, 26–33 (2018).
68. J. M. de la Rosa-Trevín *et al*., Scipion: A software framework toward integration, reproducibility and validation in 3D electron microscopy. *J. Struct. Biol.* **195**, 93–99 (2016).
69. J. L. Vilas *et al*., MonoRes: Automatic and accurate estimation of local resolution for electron microscopy maps. *Structure* **26**, 337–344.e4 (2018).
70. E. Ramírez-Aportela *et al*., Automatic local resolution-based sharpening of cryo-EM maps. *Bioinformatics* **36**, 765–772 (2020).
71. G. J. Kleywegt, T. A. Jones, xdlMAPMAN and xdlDATAMAN–Programs for reformatting, analysis and manipulation of biomacromolecular electron-density maps and reflection data sets. *Acta Crystallogr. D Biol. Crystallogr.* **52**, 826–828 (1996).
72. E. Potterton, P. Briggs, M. Turkenburg, E. Dodson, A graphical user interface to the CCP4 program suite. *Acta Crystallogr. D Biol. Crystallogr.* **59**, 1131–1137 (2003).
73. E. F. Pettersen *et al*., UCSF Chimera–A visualization system for exploratory research and analysis. *J. Comput. Chem.* **25**, 1605–1612 (2004).
74. Y. Dong *et al*., Antibody-induced uncoating of human rhinovirus B14. *Proc. Natl. Acad. Sci. U.S.A.* **114**, 8017–8022 (2017).
75. G. N. Murshudov *et al*., REFMAC5 for the refinement of macromolecular crystal structures. *Acta Crystallogr. D Biol. Crystallogr.* **67**, 355–367 (2011).
76. P. Emsley, K. Cowtan, Coot: Model-building tools for molecular graphics. *Acta Crystallogr. D Biol. Crystallogr.* **60**, 2126–2132 (2004).
77. P. D. Adams *et al*., PHENIX: A comprehensive python-based system for macromolecular structure solution. *Acta Crystallogr. D Biol. Crystallogr.* **66**, 213–221 (2010).
78. T. I. Croll, ISOLDE: A physically realistic environment for model building into low-resolution electron-density maps. *Acta Crystallogr. D Struct. Biol.* **74**, 519–530 (2018).
79. V. B. Chen *et al*., MolProbity: All-atom structure validation for macromolecular crystallography. *Acta Crystallogr. D Biol. Crystallogr.* **66**, 12–21 (2010).
80. B. A. Barad *et al*., EMRinger: Side chain-directed model and map validation for 3D cryo-electron microscopy. *Nat. Methods* **12**, 943–946 (2015).
81. C. Xiao, M. G. Rossmann, Interpretation of electron density with stereographic roadmap projections. *J. Struct. Biol.* **158**, 182–187 (2007).
82. F. Madeira *et al*., The EMBL-EBI search and sequence analysis tools APIs in 2019. *Nucleic Acids Res.* **47**, W636–W641 (2019).
83. A. M. Waterhouse, J. B. Procter, D. M. Martin, M. Clamp, G. J. Barton, Jalview Version 2–a multiple sequence alignment editor and analysis workbench. *Bioinformatics* **25**, 1189–1191 (2009).